South African Journal of Chemical Engineering 48 (2024) 425–435

Contents lists available at ScienceDirect

South African Journal of Chemical Engineering

journal homepage: www.elsevier.com/locate/sajce

Electrocatalytic overall water splitting based on $(ZnNiCoFeY)_xO_y$ high-entropy oxide supported on MoS_2

Sumayya C. Pathan [a,f], Jasmin S. Shaikh [a,b,f], Navajsharif S. Shaikh [c], Victor Márquez [b], Meena Rittiruam [a,b,d], Tinnakorn Saelee [a,b,e], Patcharaporn Khajondetchairit [a,g], Sawanta S. Mali [h], Jyoti V. Patil [h,i], Chang Kook Hong [h,i], Piyasan Praserthdam [b], Supareak Praserthdam [a,b,*]

[a] High-Performance Computing Unit (CECC-HCU), Center of Excellence on Catalysis and Catalytic Reaction Engineering (CECC), Chulalongkorn University, Bangkok, 10330, Thailand
[b] Center of Excellence on Catalysis and Catalytic Reaction Engineering (CECC), Chulalongkorn University, Bangkok, 10330, Thailand
[c] School of Materials Science and Innovation, Faculty of Science, Mahidol University, Nakhon Pathum, 73170, Thailand
[d] Rittiruam Research Group, Bangkok, 10330, Thailand
[e] Saelee Research Group, Bangkok, 10330, Thailand
[f] Shaikh Research Group, Bangkok, 10330, Thailand
[g] Khajondetchairit Research Group, Bangkok, 10330, Thailand
[h] Polymer Energy Materials Laboratory, School of Chemical Engineering, Chonnam National University, Gwangju, 61186, South Korea
[i] Optoelectronic Convergence Research Center, Chonnam National University, Gwangju, 61186, South Korea

ARTICLE INFO

Keywords:
High-entropy oxides
Hydrogen evolution reaction
Oxygen evolution reaction

ABSTRACT

Hydrogen energy is a sustainable and clean source that can meet global energy demands without adverse environmental impacts. High-entropy oxides (HEOs), multielement (5 or more) oxides with an equiatomic or near-equatomic elemental composition, offer a novel approach to designing bifunctional electrocatalysts. This work explores $(ZnNiCoFeY)_xO_y$ over MoS_2 as a bifunctional electrocatalyst (HEO–MoS_2) in an alkaline medium. The HEO was synthesized using a combustion process and loaded over MoS_2 using an ultrasonic method. The synthesized HEO over MoS2 exhibits excellent performance, including long-term stability for over 24 h, an overpotential of 214 mV vs the reversible hydrogen electrode (RHE) for the hydrogen evolution reaction (HER), and 308 mV for the oxygen evolution reaction (OER) at 10 mA cm^{-2}. This bifunctional electrocatalyst exhibits low overpotential for both the HER and the OER at high current densities. Additionally, HEO–MoS_2 demonstrates smaller solution and charge transfer resistance values. The electrolyzer was assembled using bifunctional HEO–MoS_2 electrodes for overall water splitting. These electrodes exhibited a low cell voltage of 1.65 V at 10 mA cm^{-2}. The novel electrocatalyst was fabricated using a facile and scalable method that appeals to industrial applications.

1. Introduction

Recent advancements have been achieved in the pursuit of creating readily available materials such as transition metal-based chalcogenides (e.g., MoS_2) (Zhu et al., 2019; Anjum et al., 2018), carbides (Lori et al., 2021; Lu et al., 2019), and phosphides (Shi and Zhang, 2016; El-Refaei et al., 2021) for the hydrogen evolution reaction (HER) and catalysis field (Pawar et al., 2023; Pawar et al., 2021; Charles et al., 2023; Pol et al., 2023; J.S. Shaikh et al., 2023; N.S. Shaikh et al., 2023; Shaikh et al., 2022). Additionally, researchers have explored perovskites (Beall et al., 2021; Pan et al., 2020), oxides (Burke et al., 2015), hydroxides (Burke et al., 2015), and metal sulfides (Cui et al., 2021; Wu et al., 2023) for the oxygen evolution reaction (OER). In water splitting, much of the research community tends to investigate the electrocatalytic capabilities of either the HER or OER, frequently overlooking the development of bifunctional electrocatalytic materials endowed with high catalytic efficiency (Liang et al., 2016; Sun et al., 2021).

Integrating efficient OER and HER electrocatalysts into a single

* Corresponding author.
E-mail address: supareak.p@chula.ac.th (S. Praserthdam).

https://doi.org/10.1016/j.sajce.2024.03.012
Received 12 December 2023; Received in revised form 9 March 2024; Accepted 19 March 2024
Available online 20 March 2024
1026-9185/© 2024 The Author(s). Published by Elsevier B.V. on behalf of South African Institution of Chemical Engineers. This is an open access article under the CC BY-NC-ND license (http://creativecommons.org/licenses/by-nc-nd/4.0/).

active nanostructure has emerged as a prominent topic in overall water-splitting processes (Sun et al., 2021). Heterogeneous materials comprising multiple metal components are being explored to harness the synergistic effects of electrocatalysts, resulting in superior electrocatalytic performance compared to their single-component or single-metal-based counterparts (J. Wang et al., 2021; An et al., 2019; Xiong et al., 2019). Recent advancements in this field have shown that earth-abundant electrocatalysts for the OER exhibit intrinsic activity in alkaline electrolytes compared to electrocatalysts based on Ru/Ir-based oxides/hydroxides (Han et al., 2016; Ma et al., 2015). Currently, various techniques, including heteroatom doping (Chu et al., 2020; Ma et al., 2022), nanosizing (C. Wang et al., 2021), surface engineering (Yu et al., 2023), carbon materials composites (Wu et al., 2016; Noor et al., 2021), and vacancy engineering (Yan et al., 2022; Wu et al., 2021), have been explored to improve OER catalytic performance (Suryanto et al., 2019). This is because earth-abundant transition metals (M = Co, Fe, Ni, Mo, etc.) can bind H^+ ions either strongly or weakly, leading to poor HER activity. As a result, Pt-based electrocatalysts (e.g., Pt/C) are the preferred choice for fabricating cathode electrodes to achieve low overpotentials at high current densities (Suryanto et al., 2019).

Presently, high-entropy materials (HEMs) have gained prominence as exceptionally effective catalysts for the OER (You et al., 2022; Li et al., 2021; Sha et al., 2023). This efficacy stems from the intrinsic synergy and high-entropy properties of mixed electro-catalytically active metals. Furthermore, the capacity to fine-tune their composition and surface electronic structure by incorporating various metals leads to an extensive range of potential atomic configurations on the surface of HEMs, enhancing their electrocatalytic potential. The high entropy oxides (HEOs) are constituted by at least five metals in equimolar ratios, forming a single-phase structure combined with oxygen (Rost et al., 2015). The first exploration of HEOs dates back to 2015, and since then, these materials have found applications across various domains due to their multi-faceted properties, encompassing attributes like thermal conductivity, electrochemical reactivity, and magnetic behavior (Rost et al., 2015). From a thermodynamic perspective, HEOs exhibit elevated configurational entropy due to the diverse array of elements they contain. This entropy plays a pivotal role in determining the thermodynamic stability of these materials.

Nonetheless, when compared to their counterpart, high-entropy alloys (HEAs), HEOs have received relatively limited attention within the field of high-entropy materials (HEMs), particularly concerning their application in the OER and HER. The HEO has multiple active sites. These are important because different pathways (steps) of the OER reaction have different preferred active sites for adsorption (the binding of reactant molecules/intermittents to the catalyst surface) (Kante et al., 2023). The presence of multiple active sites close together leads to a potential OER reaction without compromising other desirable properties of the electrocatalyst. For earth-abundant transition metals, high-entropy oxide leads to low overpotentials and Tafel slopes, indicating improved performance compared to standard materials such as IrOx or/and Ni/Fe layered hydroxides.

Svane et al. conducted a theoretical study on applying HEOs in the OER. In HEOs, various local environments around the active sites result in distributed adsorbed energies for intermediates, leading to lower overpotential than pure oxides (Svane and Rossmeisl, 2022). The investigation focused on a high-entropy spinel oxide with the chemical composition (Co, Cu, Fe, Mn, Ni)$_3$O$_4$. This composition exhibited limited performance, dependent on adding multi-walled carbon nanotubes (MWCNTs) (Wang et al., 2019). The high-entropy rock oxide with the composition (CoNiMnZnFe)$_3$O$_{3.2}$ has been reported to exhibit low overpotential (336 mV at 10 mA cm^{-2}), a low Tafel slope (47.5 mV dec^{-1}), and highly stable OER activity (for 20 h) in 1 M KOH (Nguyen et al., 2021). This high performance is attributed to the synergistic effect of different metal cations and the formation of a core-shell structure during activation. In this investigation, the influence of mixing perovskite halide with perovskite oxide is studied, and the enhancement in OER performance results from adding Ba–Sr–Co–Fe oxide. The high-entropy spinel oxide (CoCrFeMnNi)$_3$O$_4$ was prepared using a simple soft chemical process (Talluri et al., 2022). This electrocatalyst exhibited a low onset potential of 1.45 V vs. RHE, a low overpotential (220 mV at 10 mA cm^{-2}), and a small Tafel slope (~100 mV dec^{-1}), demonstrating its high electrocatalytic performance. However, there has been limited research on the influence of composition variations on high-entropy oxides (HEOs).

Pt-based electrocatalysts are known as HER electrocatalysts mostly because of their excellent catalytic activities; however, their high costs and limited availability limit their pragmatic application. Recently, transition metal-based HEOs have been investigated for the application of HER to overcome this problem. In the HER process, three main steps typically occur: mass diffusion, interface/surface reaction, and electron transportation. The HER process of electrocatalysts is mainly attributed to the electron transportation behavior and abilities of active metal sites. For facile electron transportation, Ding et al. reported a facile solvothermal procedure for preparing 2D HEO arrays (Ding et al., 2022). This well-aligned array of 2D structures overcomes the problem of restacking materials and facilitates the facile transportation of gas bubbles. DFT study revealed that the vacancies in HEO architectures lead to high electron densities of nearby electrocatalytic metal active sites, which enhance the electrocatalytic performance for HER.

Also, in this report, HEOs are modulated by Ar plasma post-treatment for generating oxygen vacancies on the surface of the electrocatalyst. This electrocatalyst showed low overpotential (89 mV at 10 mA cm^{-2}), small Tafel slopes (88 mV dec^{-1}), and good durability (100 h). This research showed a new strategy for engineering HEOs for the application of HER. Fan et al. reported a Pt/ (FeCoNiCrAl)$_3$O (Pt nanoparticles-HEO nanohybrid) for HER (Fan et al., 2024). The nanohybrid exhibited high HER performance with a low overpotential (22 mV at 10 mA cm^{-2}) with long-term stability (60 h) for an electrocatalytic water-splitting device.

2D transition-metal chalcogenides such as WS_2, $MoSe_2$, and MoS_2 have garnered significant attention in catalysis due to their small dimensions, unique morphologies, and chemical properties (Yin et al., 2020; Jin, 2017). The electrocatalytic activity of the transition metal chalcogenides, particularly MoS_2, has been extensively investigated for both the OER and the HER. In MoS_2 flakes, the sulfur-attached edges exhibit high electrocatalytic activity. However, despite their good catalytic activity, these metal chalcogenides face stability issues that must be addressed. Among the various approaches, forming an active interface between the sulfide matrix and co-catalyst has proven to be an effective method for improving stability. Zhang et al. reported MoS_2/-Ni_3S_2 heterostructures as an electrocatalyst for fabricating an alkali electrolyzer (Zhang et al., 2016). This device showed a low cell voltage of 1.56 V for a current density of 10 mA cm^{-2}. DFT study demonstrated that the interfaces of MoS_2 and Ni_3S_2 electrocatalysts favor the chemisorption of oxygen and hydrogen-containing intermediates, accelerating the overall water-splitting process. The MoS_2-Ni_3S_2 hetero-nanorods loaded on Ni foam were used as bifunctional electrocatalysts, which showed low overpotentials of 98 and 249 mV to reach 10 mA cm^{-2} in 1 M KOH for HER and OER, respectively (Yang et al., 2017). The hetero-nanorod electrolyser showed a low cell voltage of 1.50 V at 10 mA cm^{-2} and remarkable durability (48 h).

This research introduces a novel HEO enriched with heteroatoms (Zn, Ni, Co, Fe, and Y) that exhibits exceptional electrocatalytic capabilities for both OER and HER, thereby facilitating the overall water-splitting process. The HEO was synthesized through a straightforward combustion method and subsequently integrated with commercial MoS_2 to craft the HEO–MoS_2 nanocomposite via ultrasonication. Our investigation encompassed the OER and HER performance assessment for bare HEO, HEO–MoS_2, and MoS_2. The superior performance of HEO–MoS_2 is attributed to the synergistic effects stemming from the amalgamation of diverse metal active sites. This study introduces a rational approach to producing bifunctional catalysts through a facile and scalable approach.

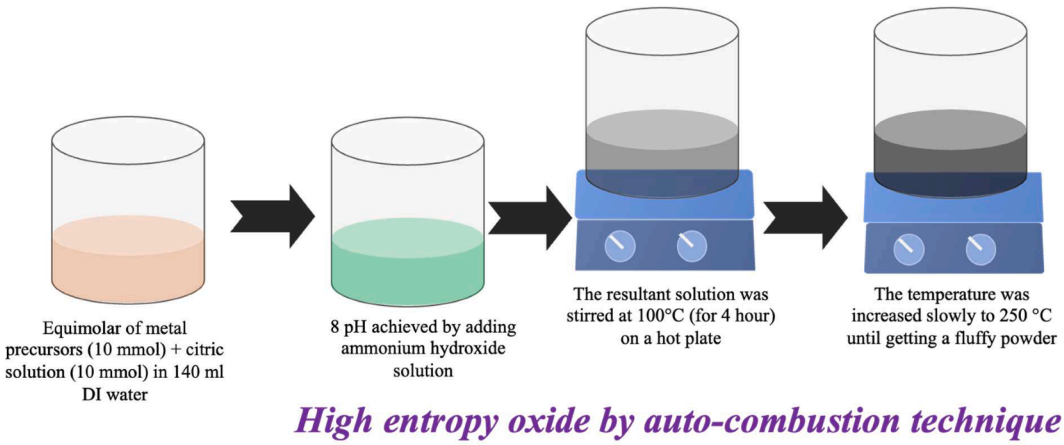

Fig. 1. The schematic representation of the synthesis of HEO by auto-combustion technique.

2. Experimental section

2.1. Chemicals

For experiments, analytical-grade metal precursors and MoS_2 were obtained from Sigma-Aldrich. Metal precursors such as zinc nitrate hexahydrate ($Zn(NO_3)_2 \cdot 6H_2O$), nickel (II) nitrate hexahydrate ($Ni(NO_3)_2 \cdot 6H_2O$), cobalt(II) nitrate hexahydrate ($Co(NO_3)_2 \cdot 6H_2O$), iron (III) nitrate nonahydrate ($Fe(NO_3)_3 \cdot 9H_2O$) and y**ttrium(III) nitrate hexahydrate ($Y(NO_3)_3 \cdot 6H_2O$)**

2.2. Synthesis of HEO

The novel HEO nanostructured powder was synthesized using the citrate gel-assisted auto-combustion technique, as depicted in Fig. 1. For this process, metal nitrates were used as precursors, and citric acid was used as a fuel and a complexing agent.

Here's a step-by-step breakdown of the procedure:

1. The metal precursors (Zn, Ni, Co, Fe, and Y nitrates, each at 10 mmol) were mixed in 140 ml of distilled water to obtain equimolar metal-nitrate solutions.
2. The citric acid powder (45 mmol) was mixed with the metal precursor solution to form a xerogel.
3. The pH of the resulting solution was maintained at 8 using an ammonium hydroxide solution.
4. The solution was stirred at 100 °C for 4 h on a hot plate.

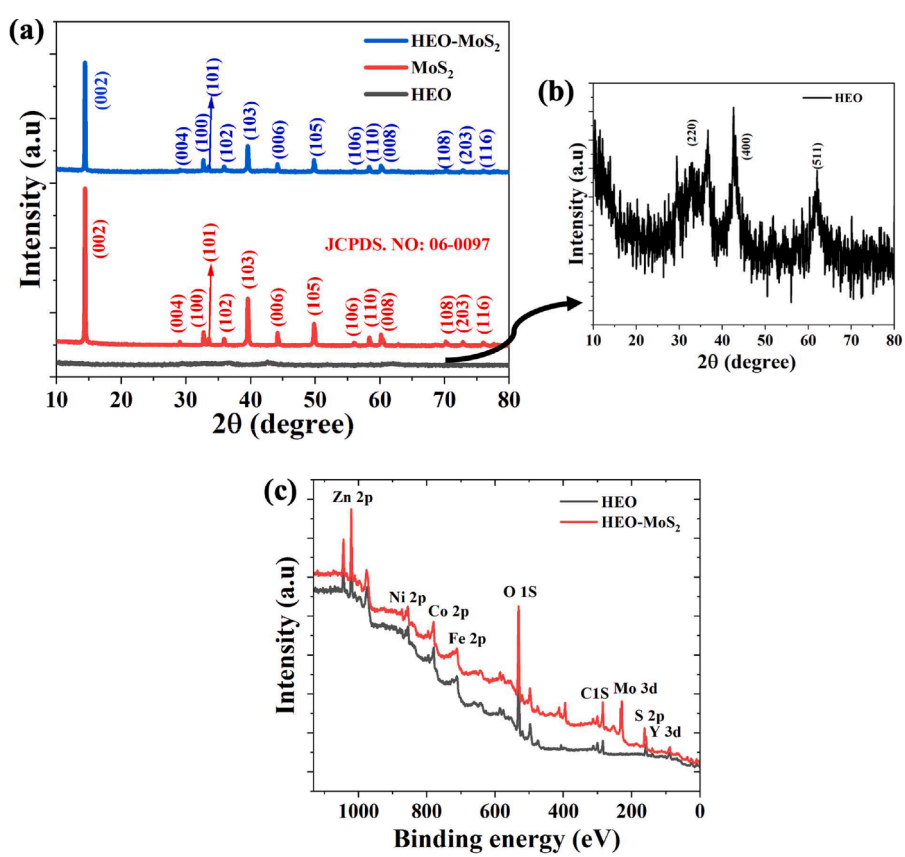

Fig. 2. (a) XRD pattern of HEO, MoS_2 and HEO–MoS_2, (b) XRD of HEO, and (c) survey spectrum of HEO and HEO–MoS_2 powders.

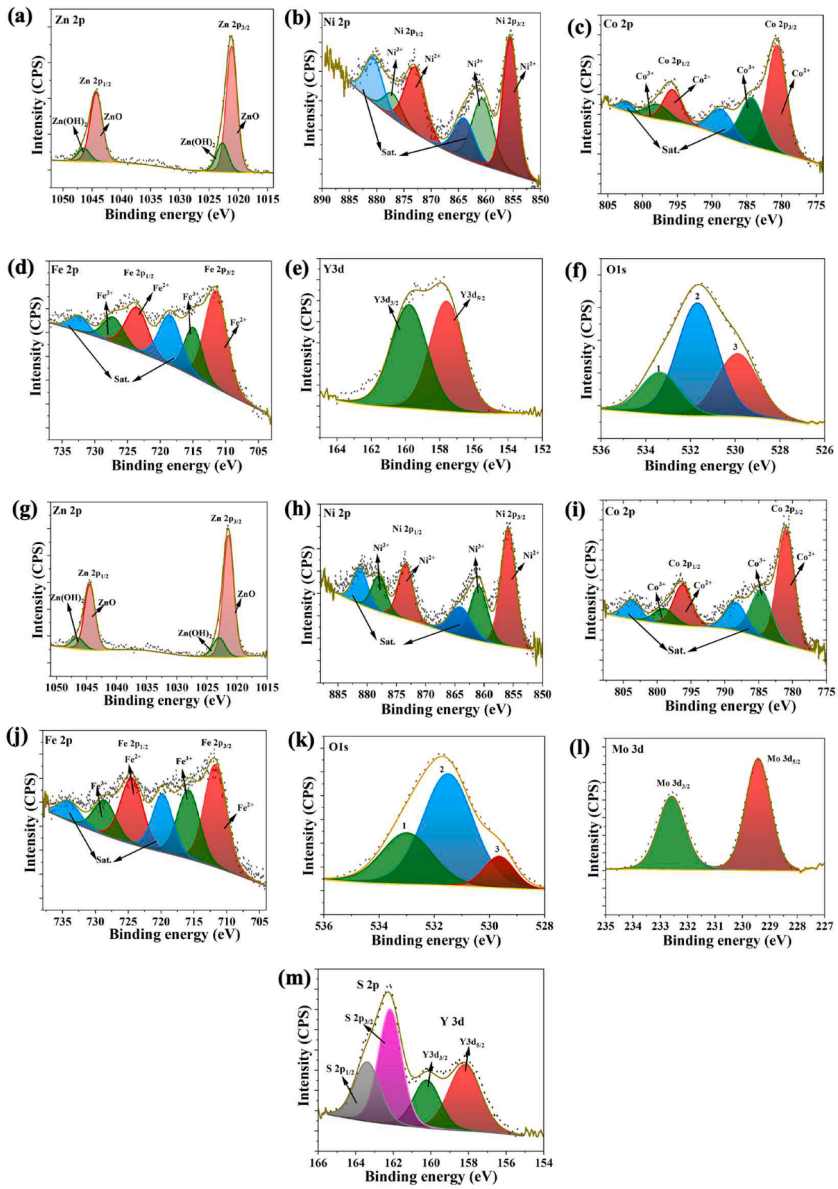

Fig. 3. The high-resolution XPS spectra of HEO powder for (a) Zn 2p, (b) Ni 2p, (c) Co 2p, (d) Fe 2p, (e) Y 3d, (f) O 1s and HEO–MoS_2 powder for (g) Zn 2p, (h) Ni 2p, (i) Co 2p, (j) Fe 2p, (k) O 1s, (l) Mo 3d, and (m) S 2p and Y 3d.

5. After the gelation process, the temperature was increased to 250 °C until the soft powdery solid formed.
6. Finally, the resulting powder was pulverized using a mortar and pestle.

2.3. Synthesis of HEO–MoS_2

We mixed HEO and MoS_2 in a 1:1 wt ratio (0. 120 g of HEO: 0.120 g of MoS_2) and added them to 10 ml of distilled water. The mixture was then sonicated for 30 min to achieve uniform dispersion. Subsequently, the resulting solution was left at room temperature for 5 days to allow the water to evaporate. The resulting powder is the HEO–MoS_2 nanocomposite.

2.4. Material characterizations

We conducted XRD characterizations using a D/MAX Ultima III XRD spectrometer (Rigaku, Japan) with a Cu Kα line (1.5410 Å). The elemental compositions of the catalysts were analyzed using XPS (VG Multilab 2000-Thermo Scientific USA, K-Alpha) with photon energies ranging from 0.1 to 3 keV. Surface morphology studies were performed with a scanning electron microscope (SEM; S4700, Hitachi). Electron mapping of the catalysts was performed using energy-dispersive X-ray (EDX) in scanning transmission electron microscopy (STEM) mode.

2.5. Electrochemical measurements

To prepare the electrocatalyst ink, 40 mg was uniformly dispersed in 160 μL of deionized water, mixed with 80 μL of Nafion (5 wt%) solution, and sonicated to achieve a homogeneous mixture. After ink formation, 30 μL of the electrocatalyst ink was deposited onto the Ni foam and then dried at 80 °C for half an hour for subsequent electrochemical measurements.

All electrochemical characterizations were conducted using a PGSTAT Autolab electrochemical workstation at room temperature in a three-electrode system with 1 M KOH. Before testing, the KOH solution was exposed to N_2 bubbles for half an hour. The working electrode was a Ni foam coated with the electrocatalyst, while a Hg/HgO electrode

Table 1
The binding energy of deconvoluted peaks of HEO and HEO–MoS_2.

		HEO (eV)					HEO–MoS_2 (eV)				
		$2p_{3/2}$	$2p_{1/2}$	$3d_{5/2}$	$3d_{3/2}$	1s	$2p_{3/2}$	$2p_{1/2}$	$3d_{5/2}$	$3d_{3/2}$	1s
Zn	2+	1021.2	1044.3				1021.4	1044.5			
Ni	2+	855.6	873.0				855.9	873.4			
	3+	860.7	877.3				861.0	878.0			
Co	2+	781.0	795.7				781.1	796.1			
	3+	784.4	798.0				784.7	799.1			
Fe	2+	711.6	723.7				711.7	724.6			
	3+	715.0	727.4				715.8	728.8			
Y				157.6	159.8				158.1	160.2	
O	O1					533.4					533.0
	O2					531.7					531.5
	O3					529.9					529.7
Mo	4+								229.4	232.6	
S	2-						162.2	163.4			

served as the reference electrode, and a graphite bar was used as the counter electrode. Current density measurements were normalized to a geometrical area of 1 cm^2. We used the Nernst equation to convert electrode potentials to the reversible hydrogen electrode (RHE). The potential, denoted as $E_{Hg/HgO}$, was converted to the RHE potential, denoted as E_{RHE}, using the following equation (Zhang et al., 2023).

$$E(V \text{ vs RHE}) = E^{o}_{Hg/HgO} + E_{Hg/HgO} + 0.0591 \text{ X pH} \quad (1)$$

Where, $E_{Hg/HgO}$ referred to as measured potential vs. the Hg/HgO reference electrode $E^{o}_{Hg/HgO} = 0.098\ V$. The common method used to benchmark value determination is the overpotential value to deliver a 10 mA cm^{-2} current density, the resultant value of a solar water splitting cell with 10 % conversion efficiency.

The overpotential (η) of OER electrode was measured at 10 mA cm^{-2} via the following relation (Shaikh et al., 2022),

$$\eta = E_{RHE} - 1.23 \quad (2)$$

The working electrode was pre-activated by subjecting it to 250 cycles of cyclic voltammetry (CV) at 100 mV/s before the electrochemical experiments.

3. Results and discussion

3.1. Structural characterization

In Fig. 2a, the XRD patterns of the HEO, MoS_2 and HEO–MoS_2 are presented. The XRD peaks of MoS_2 at 2θ = 14.3°, 29.0, 33.0, 33.5, 36.0, 40.0,44.2, 50.0, 56.1, 58.3, 60.2, 70.2, 72.9, and 76.0 correspond to the reflections of planes (002), (004), (100), (101), (102), (103), (006), (105), (106), (110), (008), (108), (203) and (116) respectively, indicating the presence of the of MoS_2 (JCPDS card no. 06-0097) (Nagarajan et al., 2022). The XRD peaks at 2θ = 14.3, 29.0, 33.0, 34.0, 36.0, 39.5, 44.2, 50.0, 56.1, 58.4, 60.3, 70.1, 73.0, and 76.0 correspond to the planes (002), (004), (100), (101), (102), (103), (006), (105), (106), (110), (008), (108), (203), and (116), respectively, indicating the presence of MoS2 in HEO–MoS2 sample (JCPDS card no. 06–0097). Here, HEO–MoS_2 lacks HEO peaks due to the amorphous-like structure of HEO and has a less intense peak than MoS_2 peaks. The XRD pattern of bare HEO ($(ZnNiCoFeY)_xO_y$) reveals broad peaks at 2θ values of 35.2°, 42.5°, and 61.2°, corresponding to the (220), (400), and (511) planes, respectively (JCPDS no. 23-1237 and PDF no. 9,002,321) (Talluri et al., 2022). This result confirms the formation of a single-phase spinel HEO (Fig. 2b).

3.2. X-ray photoelectron spectroscopy studies

X-ray Photoelectron Spectroscopy (XPS) was employed to characterize HEO and HEO–MoS_2, allowing us to study the surface composition and elemental valences. Fig. 3c shows the survey spectra of HEO and HEO–MoS_2 and reveals the presence of Zn, Ni, Co, Fe, Y, and O in HEO and Zn, Ni, Co, Fe, Y, O, Mo, and S in HEO–MoS_2. The Zn 2p XPS spectrum is deconvoluted and obtained two peaks at 1021.2 eV (Zn $2p_{3/2}$) and 1044.3 eV (Zn $2p_{1/2}$) revealed that the presence of Zn^{2+} in HEO (Fig. 3a) (Claros et al., 2020). The Ni 2p XPS spectrum is deconvoluted and obtained peaks consist of Ni $2p_{3/2}$, Ni $2p_{1/2}$, and satellite peaks (Fig. 3b). The two peaks observed at 855.6 eV and 873.0 eV reveal the presence of Ni^{2+}. Also, two satellite peaks are observed at 864.0 eV and 880.8 eV. The satellite peaks confirm the presence of Ni^{2+}. In addition, two more peaks are observed at 860.7 eV and 877.3 eV, revealing the presence of Ni^{3+} (Wang et al., 2020). The XPS spectrum of Co 2p consists of two peaks: Co $2p_{3/2}$ and Co $2p_{1/2}$ (Fig. 3c). The Co $2p_{3/2}$ spectrum can be deconvoluted and observed with two peaks at 781.0 eV and 784.4 eV. The Co $2p_{1/2}$ spectrum can be deconvoluted and found with two peaks at 795.7 eV and 798.0 eV. The peaks 781.0 eV and 795.7 eV are attributed to the Co^{2+}, while two other peaks at 784.4 eV and 798.0 eV reveal the presence of Co^{3+}. In addition, two satellite peaks are observed at 788.8 eV and 802.5 eV (Wang et al., 2020). The Fe 2p XPS spectrum consists of two peaks, Fe $2p_{3/2}$ and Fe $2p_{1/2}$ (Fig. 3d). The Fe $2p_{3/2}$ spectrum can be deconvoluted into two peaks centered at 711.6 eV and 715.0 eV. The Fe $2p_{1/2}$ has two peaks centered at 723.7 eV and 727.4 eV. The two peaks mentioned above at 711.6 eV and 723.7 eV correspond to Fe^{2+}, and those at 715.0 eV and 727.4 eV correspond to Fe^{3+} (Wang et al., 2020). The XPS spectrum of Y 3d consists of two prominent peaks: (1) at 157.6 eV (Y $3d_{5/2}$) and (2) at 159.8 eV (Y $3d_{3/2}$) (Fig. 3e) (Suturin et al., 2018).

According to various works, oxygen vacancies in metal oxides benefit both OER and HER reactions and can be useful in HEO–MoS_2. Oxygen vacancies promote the adsorption/desorption of oxygen species and the mass transportation process. Therefore, the O1s XPS spectrum of HEO–MoS_2 is further investigated (Fig. 3f). The O1s high-resolution spectrum of HEO–MoS_2 exhibits three peaks centered at 533.4 (O1), 531.7 (O2), and 529.9 eV (O3), respectively, which are attributed to lattice oxygen (O1), defect sites having low oxygen coordination (O2) and chemisorption or physically adsorption of water molecules on the surface of catalyst (O3) (Danyang et al., 2022). The following equation estimates the peak areal percentage that calculates oxygen vacancies in HEO–MoS_2.

$$\text{Percentage } \% = \frac{O2}{O1 + O2 + O3} \times 100\ \% \quad (3)$$

In HEO, the 52.25 % oxygen vacancies are present. Similarly, the high resolution of (Fig. 3g) Zn 2p, (Fig. 3h) Ni 2p, (Fig. 3i) Co 2p, (Fig. 3j) Fe 2p, (Fig. 3k) O1s revealed the presence of elements mentioned above in HEO–MoS_2. The high-resolution spectrum of Mo 3d shows two prominent peaks centered at 229.4 eV (Mo $3d_{5/2}$) and 232.6 eV (Mo $3d_{3/2}$) that occurred for Mo^{4+} in HEO–MoS_2 nanocomposites (Fig. 3l) (Amin et al., 2018). The high-resolution spectrum of S 2p consists of two peaks centered at 162.2 eV (S $2p_{3/2}$) and 163.3 eV (S

Table 2
The XPS atomic ratios of M^{2+}/M^{3+} in HEO and HEO–MoS_2.

Sample name	(Ni^{2+}/Ni^{3+}) of $2p_{3/2}$	(Co^{2+}/Co^{3+}) of $2p_{3/2}$	(Fe^{2+}/Fe^{3+}) of $2p_{3/2}$
Sample Name	**(Ni^{2+}/Ni^{3+})**	**(Co^{2+}/Co^{3+})**	**(Fe^{2+}/Fe^{3+})**
HEO	49.28/18.45 = (2.67:1) ≈ **2:1**	54.09/30.38 = (1.78:1) ≈ **2:1**	52.8/23.51 = (2.24:1) ≈ **2:1**
HEO–MoS_2	48.98/28.29 = (1.73:1) ≈ **2:1**	54.64/26.63 = (2.05:1) ≈ **2:1**	48.86/30.07 = (1.62:1) ≈ **2:1**

Table 3
The atomic percentage of elements in HEO and HEO–MoS_2.

Elements	Atomic percentage of HEO	Atomic percentage of HEO–MoS_2
O 1s	24.17	17.71
Fe 2p	16.06	16.4
Co 2p	13.70	17.36
Ni 2p	16.38	13.37
Zn 2p	25.41	22.09
Y 3d	4.28	4.74
Mo 3d	**NA**	1.25
S 2p	**NA**	2.1

$2p_{1/2}$), revealing the presence of S^{2-} and the XPS spectrum of Y 3d consists of two prominent peaks: (1) at 158.1 eV (Y $3d_{5/2}$) and (2) at 160.2 eV (Y $3d_{3/2}$) in HEO–MoS_2 (Fig. 3m) (Li et al., 2017). In HEO–MoS_2, 61.0 % oxygen vacancies are present, which is higher than that of HEO. In summary, Ni, Co, and Fe elements showed a mixed valence state, while other elements of HEO and HEO–MoS_2 showed a single valence state. Table 1 consists of the binding energy of deconvoluted peaks of the elements mentioned above in HEO and HEO–MoS_2. The XPS atomic ratios of M^{2+}/M^{3+} in HEO and HEO–MoS_2 are included (**see** Table 2). The ratios of the oxidation state for HEO–MoS_2 are different from HEO. When the MoS_2 is included, the Fe^{+3} ratio is increased. This could be caused by the increased electron affinity of the S from the MoS_2, causing an oxidation of the Iron. The S atom can draw more electrons than the O atom, while the Fe atom gives them electrons transitioning from Fe^{+2} to Fe^{+3}, distorting the spinel structure (Mayhall et al., 2011). The presence of metal ions having higher valence states is highly conducive to the adsorption process of intermediates (e.g.,*OH, *OOH), which can improve the OER kinetics (He et al., 2024). Table 3 consists of the atomic weight percentage of HEO and HEO–MoS_2, which are illustrated in **Figure S1a** and **Figure S1b**, respectively.

3.3. Surface morphology study

Fig. 4a and b show SEM images of the HEO–MoS_2, revealing the presence of a porous surface. Fig. 4c displays the EDS spectrum of HEO–MoS_2, indicating the presence of Zn, Ni, Co, Fe, Y, O, Mo, and S elements. The inset table in Fig. 4c shows the weight and atomic percentages of all elements in HEO–MoS_2. Based on the elemental atomic percentages of HEO–MoS_2, XRD study (spinel crystal structure), and the presence of oxygen vacancies (from XPS studies), we calculated the stoichiometry which consists of $(Fe_{0.20}, Co_{0.22}, Ni_{0.20}, Zn_{0.22}, Y_{0.14})_3O_{4-y}$–$MoS_2$. Fig. 5a shows the dark-field STEM image (HAADF STEM image) of HEO–MoS_2 and corresponding EDS mapping reveals the presence of uniform elemental distribution of (Fig. 5b) Zn, (Fig. 5c) Ni, (Fig. 5d) Co, (Fig. 5e) Fe, (Fig. 5f) Y, (Fig. 5g) O, (Fig. 5h) Mo, (Fig. 5i) S in the HEO–MoS_2 catalyst powder reveals the formation of HEO and its nanocomposite with MoS_2.

3.4. HER electrocatalysis of HEO, HEO–MOS_2, and MoS_2

The electrocatalytic performance of HEO, HEO–MoS_2, and MoS_2 were evaluated. Before the electrochemical tests, stable state electrocatalysts (HEO–MoS_2, HEO, and MoS_2) were achieved by 250 cycles of CV at a 100 mV s^{-1} between 0 and 0.6 V vs. Hg/HgO in the 1 M KOH electrolyte.

The electrochemical active surface area (ECSA) measures active site density. It was estimated by the electrochemical double-layer capacitance (Cdl). The Cdl of the HEO–MoS_2 electrode was estimated by carrying out CV (non-Faradaic region) from 0.2 to 0.4 V (vs. Hg/HgO)

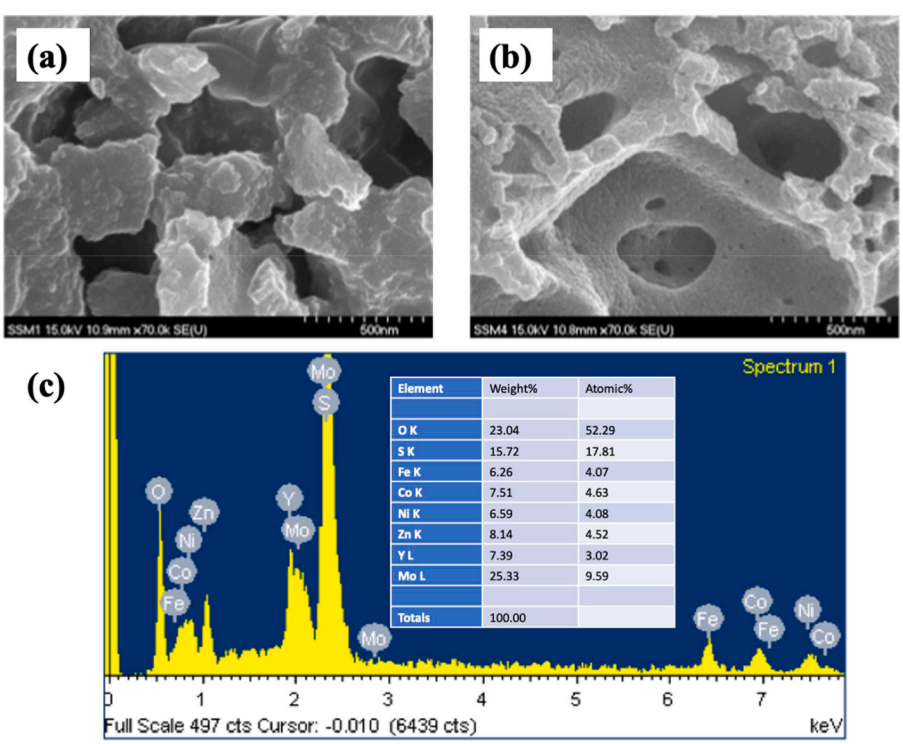

Fig. 4. (a and b) FE-SEM images of the HEO–MoS_2 powder. (c) EDS spectrum of the HEO–MoS_2 powder.

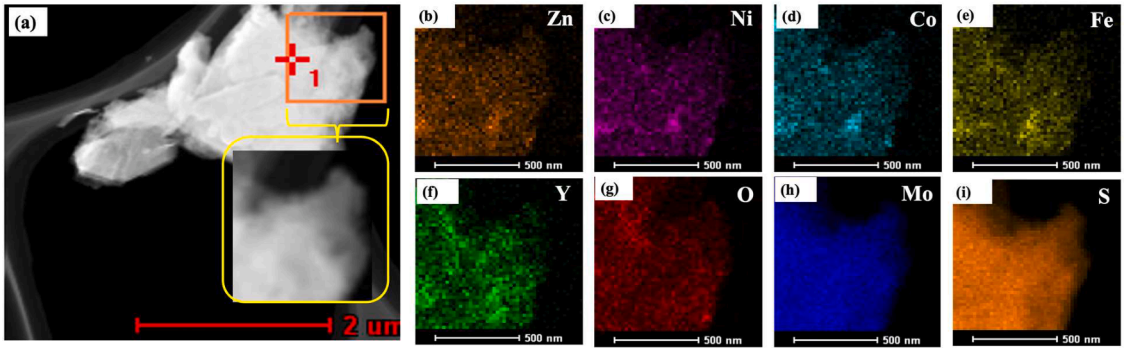

Fig. 5. (a) HAADF STEM image of powder HEO–MoS_2 powder and corresponding EDS mapping of (b) Zn, (c) Ni, (d) Co, (e) Fe, (f) Y, (g) O, (h) Mo, (i) S in the powder HEO–MoS_2 catalyst.

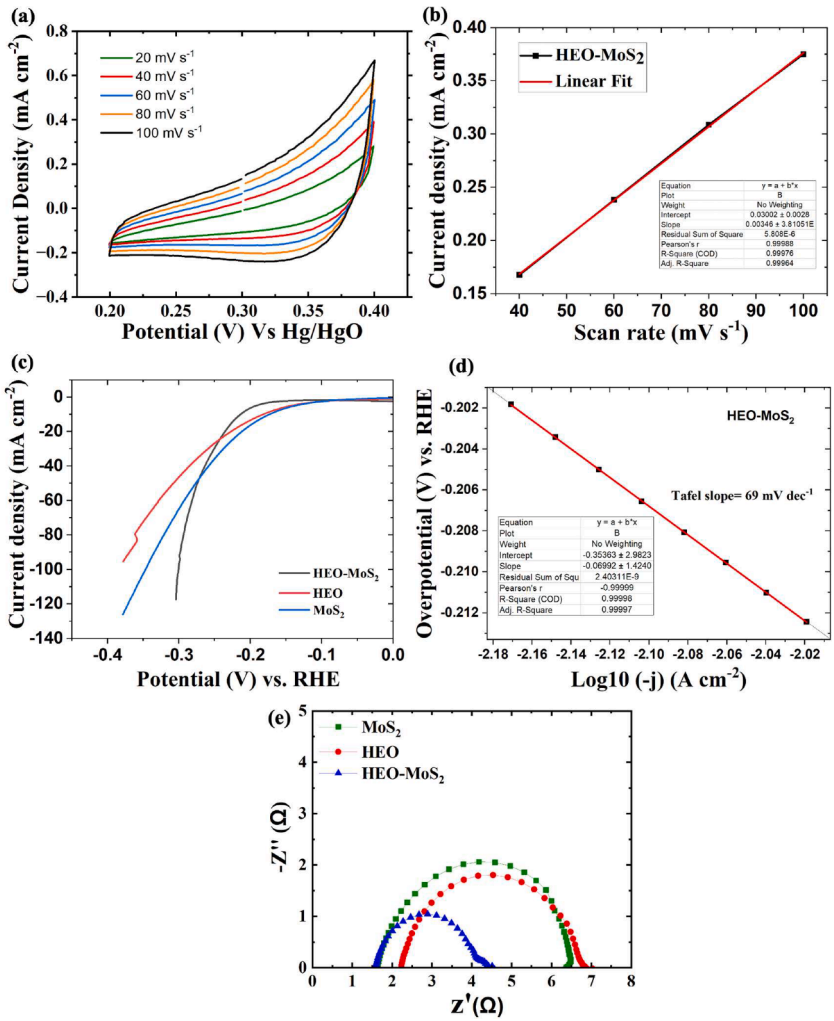

Fig. 6. (a) CVs of HEO–MoS_2 measured at a non-Faradic region (0.20–0.40 V vs. Hg/HgO) at different scan rates for the calculation of ESCA, (b) The plot of capacitive current density vs. scan rate is plotted for HEO–MoS_2, (c) LSVs of HEO–MoS_2, MoS_2, and HEO for HER characteristics (d) Tafel plot HEO–MoS_2, (e) Nyquist plots for HEO–MoS_2, MoS_2, and HEO recorded at overpotential for −10 mA cm^{-2} of LSVs.

under distinct scan rates (Fig. 6a). The plot of (J_a–J_c) (mA cm^{-2}) vs. scan rate (mV s^{-1}) for HEO–MoS_2 is shown in Fig. 6b. The slope of this plot is used to calculate Cdl. The relation between slope and Cdl is Cdl = slope/2. The ECSA was estimated by dividing the Cdl by a specific capacitance (S_{cp}) of a flat surface (440 μF cm^{-2}). ECSA is estimated via the following relation (Shaikh et al., 2022),

$$\mathrm{ECSA} = \frac{\mathrm{Cdl}}{40\ \mu\mathrm{F\ cm^{-2}}} \tag{4}$$

In the case of HEO–MoS_2, the Cdl value stands at 1.73 mF cm^{-2}, and the ECSA measures 43 cm^2. To estimate the Cdl of the HEO electrode, we conducted cyclic voltammetry (CV) in the non-Faradaic region within the voltage range of 0.2–0.4 V (vs. Hg/HgO) at various scan rates, as

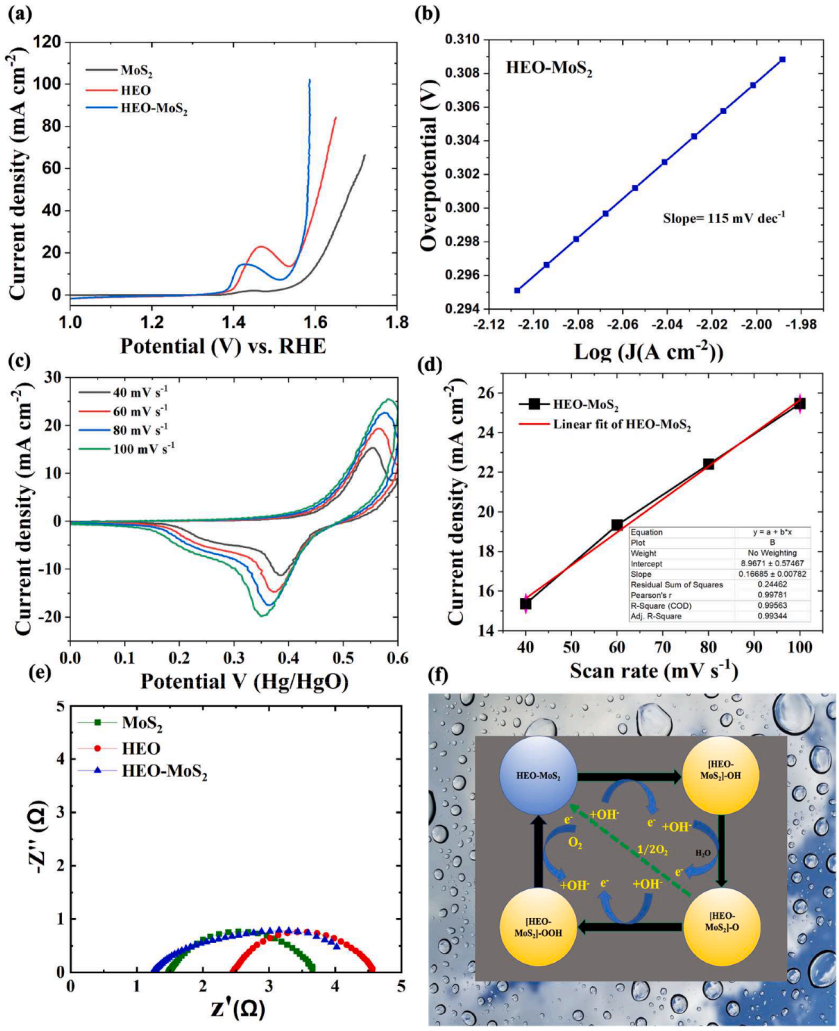

Fig. 7. (a) LSVs of HEO–MoS_2, MoS_2, and HEO for OER characteristics (b) corresponding Tafel plot HEO–MoS_2, (c) CVs of the HEO–MoS_2 at different scan rates. (d) The plot of peak current density (mA cm^{-2}) of oxidation region of CV vs. scan rates (mV s^{-1}) of HEO–MoS_2. The linear slope of HEO–MoS_2 is used to estimate active species (m) and corresponding TOF values. (e) Nyquist plots for HEO–MoS_2, MoS_2, and HEO were recorded at overpotential for 10 mA cm^{-2} LSVs. (f) The schematic representation of the OER mechanism of HEO–MoS_2.

shown in **Figure S2a**. Furthermore, the ECSA was determined for HEO, yielding a value of 104 cm^2, as depicted in **Figure S2b**. The Cdl of the MoS_2 electrode was estimated by carrying out CV (non-Faradaic region) from −0.20 to 0 V (vs. Hg/HgO) and under distinct scan rates (**Figure S2c**). The ECSA was calculated for MoS_2, and its value is 5.65 cm^2 (**Figure S2d**). The LSVs with 90 % iR correction (by using open circuit potential-based EIS) of the materials mentioned above are shown in (Fig. 6c). The HEO–MoS_2 exhibits the approximately 214 mV overpotential for −10 mA cm^{-2} current density, which is higher than that of MoS_2 (174 mV) and HEO (185 mV). However, at a high current density of −80 mA cm^{-2}, the overpotential of 293 mV is required for HEO–MoS_2, which is substantially smaller than those of HEO (360 mV) and MoS_2 (321 mV). The high performance of HEO–MoS_2 at high current density confirms its pragmatic application. The Tafel plots were calculated by using LSVs of the materials mentioned above. The Tafel slopes of the HEO–MoS_2 (Fig. 6d), HEO (**Figure S3a**), and MoS_2 (**Figure S3b**) are 69, 130, and 215 mV per decade, respectively. The Tafel slope shows the inherent characteristic of the catalyst that is estimated by the rate-limiting step. The Tafel plots are used to explore the kinetics of the HER, and a smaller Tafel slope of HEO–MoS_2 confirms a favorable kinetics of the HER reaction. The low Tafel slope of HEO–MoS_2 signifies a Volmer–Heyrovsky mechanism and a rate-determining step for the desorption process of the discharged proton. The HEO–MoS_2 material exhibits a smaller overpotential at high current density and low Tafel slope, suggesting high performance compared to HEO and MoS_2. We also examined EIS measurements at overpotential (η_{10}) to get insight into electrode-electrolyte kinetics during the HER reaction. Nyquist plots of the materials mentioned above are shown in Fig. 6e, the HEO–MoS_2 material has the smallest Rct (4.4 Ω) than that of HEO (6.9 Ω) and MoS_2 (6.3 Ω), confirming a faster and facile HER kinetics.

3.5. OER electrocatalysis of HEO, HEO–MoS_2, and MoS_2

The OER process at the anode electrode is a sluggish half-reaction in water splitting. The OER reaction occurs via a complex four-step proton-coupled electron transportation reaction and is the thermodynamically and kinetically rate-limiting process. The high OER performance of the electrocatalyst is strongly dependent on the architecture of the current collector. The electrocatalyst performs significantly better when put on a 3D porous structural current collector. Hence, nickel foam was employed to load the catalyst. The OER process is tested using a three-electrode setup (graphite cathode electrode, Hg/HgO reference electrode, and working electrode (catalyst)) with an N_2-saturated KOH electrolyte. The OER (electrocatalytic) performance of HEO–MoS_2 was compared to HEO and commercial MoS_2 in 1 M KOH. The intention was to enhance the catalyst activity and remove unstable particles of metal

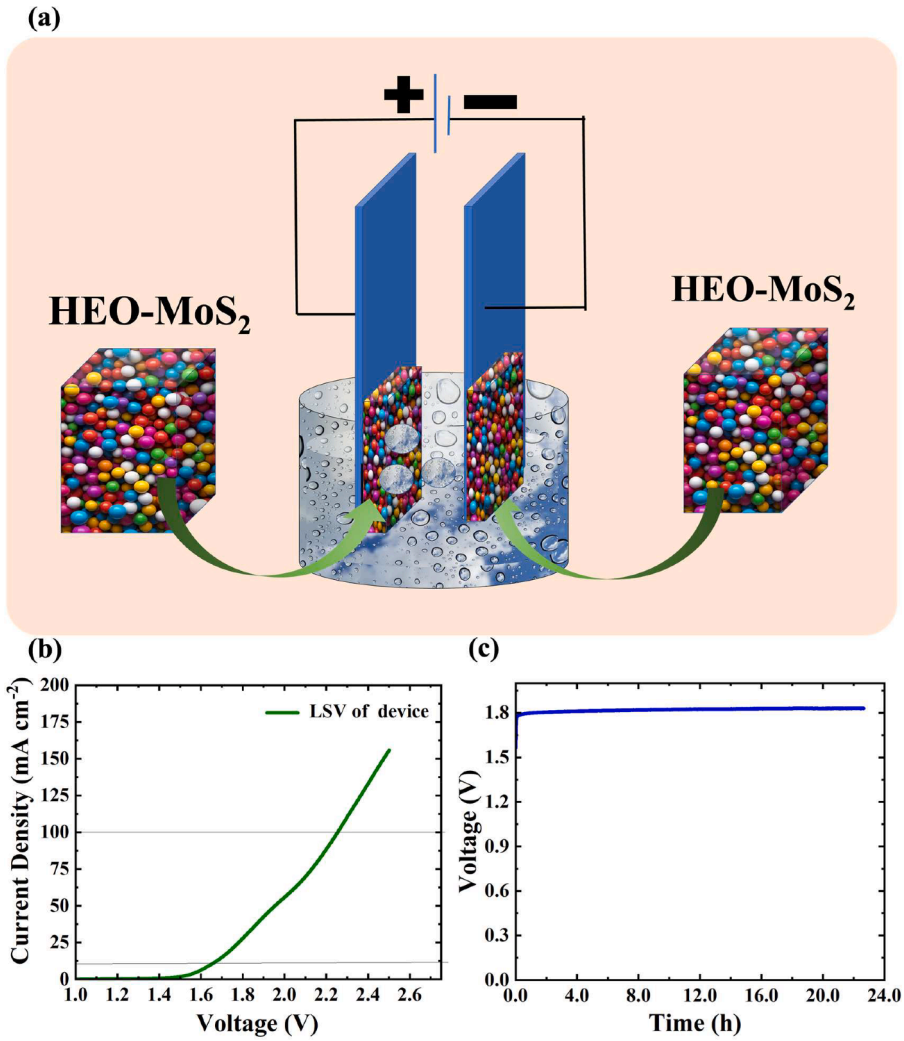

Fig. 8. (a) The overall water splitting device (two-electrode system) of HEO–MoS_2 electrodes. (b) LSV of the device mentioned above. (c) Chrono-potentiometric analysis of HEO–MoS_2 based device.

species. LSVs were measured at 5 mVs^{-1} from 1.0 to 1.8 V vs RHE in alkaline media (KOH electrolyte), respectively, with 90 % iR correction. The current density was normalized over the geometric surface area of the electrode (1 cm^2). The OER performance of the HEO, HEO–MoS_2, and MoS_2 were investigated in the electrochemical parameters. The overpotential of HEO–MoS_2 and MoS_2 are 308 and 356 mV, respectively, reaching 10 mA cm^{-2} (Fig. 7a). HEO does not have overpotential at 10 mA cm^{-2} due to a broad redox peak. HEO–MoS_2, HEO, and MoS_2 overpotentials are 352, 380, and 454 mV for a high current density of 50 mA cm^{-2}, respectively. The high performance of HEO–MoS_2 is attributed to increased active sites and improved conductivity by adding MoS_2. The OER performance of commercial MoS_2 is poor.

The Tafel slope is commonly employed to determine the electrochemical reaction mechanism and evaluate the OER kinetics. Tafel slopes around 21–120 mV dec^{-1} can be reached by the rate-determining step and intermediate coverage degree, which changes to the overpotential. Due to this, the low-overpotential and high overpotential could produce distinct Tafel slopes even for the identical rate-determination step. Hence, it is very challenging to determine the rate-determination step based alone on the Tafel slope. However, it can be safe to say that a lesser Tafel slope reflects the presence of the rate-determination step at the ending part of the OER. A lesser Tafel slope is more beneficial for water oxidation since it produces a radical enlarged OER current concerning overpotential. The good catalytic kinetic of HEO–MoS_2 was confirmed by the small Tafel slope 115 mV dec^{-1} (Fig. 7b) as compared to MoS_2 (119 mV dec^{-1}) (**Figure S3**).

To assess the intrinsic OER activity of HEO–MoS_2, we calculate the turnover frequency (TOF), which quantifies the number of moles of O_2 generated per unit of time at a specific overpotential. Calculating TOF requires determining the concentration of active sites via electrochemical means. We conducted cyclic voltammetry (CV) experiments on HEO–MoS_2 in the potential range of 0–0.6 V vs. Hg/HgO, as illustrated in Fig. 7c. To estimate the number of active sites (denoted as "*m*") within HEO–MoS_2, we plotted the peak current density (oxidation peak) mA cm^{-2} against the scan rate (mV/s), revealing a linear relationship, as shown in Fig. 7d. This plot was linearly fitted and got Pearson's correlation coefficient = 0.99781, and the R-square was 0.99463. The m evaluation is done by the relation in Eq. (5) (Shaikh et al., 2022):

$$\text{Slope} = \frac{n^2F^2m}{4RT} \tag{5}$$

Where *n* is the number of electrons transported (here, one electron process is assumed), *F* is the Faradic constant (96,485 C.mol), *R* is the ideal gas constant, and *T* is the absolute temperature. The TOF of the HEO–MoS_2 electrode is estimated via the following relation (Shaikh et al., 2022):

$$\text{TOF} = \frac{JA}{4Fm} \tag{6}$$

Where *J* is a current density at an overpotential of 350 mV, and A is

the geometrical area of the electrode. The 4 constant numbers represent the electrons required for 1 mole of O_2 molecule evolution. The estimated TOF value is higher for HEO–MoS_2 (0.589 mol O_2 per S) as compared to HEO (0.529 mol O_2 per S) (**Figure S5 a and b**) and MoS_2 (0.212 mol O_2 per S) (**Figure S 5c and d**). This result confirmed the high intrinsic catalytic property of HEO–MoS_2.

The impedance was conducted at 1.538 V vs RHE, and the Nyquist plot of HEO–MoS_2 exhibited a low charge-transfer resistance (4.39 Ω) (Fig. 7e). This result confirmed that HEO–MoS_2 exhibited good catalytic kinetics for water dissociation and the OER. In OER reaction, a four-electron transport process occurs, resulting in the required high overpotential for water splitting and a large energy loss. As per the above-discussed results, the OER performance of HEO–MoS_2 can occur following the proposed mechanism in 1 M KOH. In this OER process, (HEO–MoS_2)–O, (HEO–MoS_2)–OOH type (here HEO–MoS_2 is the active surface site) intermittent are contributed to the charge-transporting process. The proposed mechanism of the HEO–MoS_2 catalyst under 1 M KOH is demonstrated in Fig. 7f, and the proposed reactions can occur as follows (He et al., 2023).

$$[\mathrm{HEO-MoS_2}] + \mathrm{OH^-} \rightarrow [\mathrm{HEO-MoS_2}]\mathrm{OH} + \mathrm{e^-} \quad (7)$$

$$[\mathrm{HEO-MoS_2}]\mathrm{OH} + \mathrm{OH^-} \rightarrow [\mathrm{HEO-MoS_2}]\mathrm{O} + \mathrm{H_2O} + \mathrm{e^-} \quad (8)$$

$$2[\mathrm{HEO-MoS_2}]\mathrm{O} \rightarrow 2[\mathrm{HEO-MoS_2}] + \mathrm{O_2} \quad (9)$$

$$[\mathrm{HEO-MoS_2}]\mathrm{O} + \mathrm{OH^-} \rightarrow [\mathrm{HEO-MoS_2}]\mathrm{OOH} + \mathrm{e^-} \quad (10)$$

$$[\mathrm{HEO-MoS_2}]\mathrm{OOH} + \mathrm{OH^-} \rightarrow [\mathrm{HEO-MoS_2}] + \mathrm{O_2} + \mathrm{H_2O} + \mathrm{e^-} \quad (11)$$

Taking inspiration from the remarkable electrocatalytic performance of HEO–MoS_2 for both the OER and the HER in alkaline conditions, we extended the application of this bifunctional catalyst to electrochemical overall water splitting using a single two-electrode electrolyzer in an alkaline environment (1 M KOH), as depicted in Fig. 8a. Fig. 8b illustrates the LSV analyzed at a scan rate of 5 mV s^{-1}. Notably, this catalyst demonstrates a current density of 10 mA cm^{-2} at an impressively low cell voltage of 1.65 V while achieving current densities of 50, 80, and 100 mA cm^{-2} at 1.96, 2.16, and 2.25 V, respectively. This exceptional performance in the electrolyzer can be attributed to the catalyst's ability to integrate the OER and HER properties seamlessly, leveraging the synergistic effects of its elemental composition. To assess its durability for overall water splitting, a chronopotentiometric stability study was conducted over 23 h at 10 mA cm^{-2} (Fig. 8c). The results demonstrated a minimal loss in voltage, indicating a high degree of stability for sustained overall water-splitting performance.

4. Conclusions

In summary, we have successfully synthesized the high-entropy oxide-MoS_2 nanocomposite via a straightforward wet chemical route. The resultant HEO–MoS_2 showcased remarkable performance in the HER and the OER under alkaline conditions. Moreover, it exhibited exceptional overall water-splitting capabilities, achieving a voltage of 1.65 V at a current density of 10 mA cm^{-2}. These significant findings have the potential to pave the way for advancements in the field of heterogeneous electrocatalysis. The advantages of HEO–MoS_2 heterostructures for the high-performance electrolyzer for overall water splitting will open new possibilities to develop novel HEMs and rational engineering of nanostructures and interfaces.

Declaration of competing interest

The authors declare that they have no known competing financial interests or personal relationships that could have appeared to influence the work reported in this paper.

Acknowledgments

All authors highly acknowledged that this research was supported by the Second Century Fund (C2F). Also, the following funding is acknowledged: 1) Thailand Science Research and Innovation Fund Chulalongkorn University (No. 6641/2566), 2) National Science and Technology Development Agency, Thailand, 3) the NSRF via the Program Management Unit for Human Resources & Institutional Development, Research, and Innovation [Grant No. B16F640143 and B13F6654], and 4) Hub of Knowledge funding National Research Council of Thailand (NRCT).

Supplementary materials

Supplementary data associated with this article can be found, in the online version, at 10.1016/j.sajce.2024.03.012.

References

Amin, R., Hossain, M.A., Zakaria, Y., 2018. Interfacial kinetics and ionic diffusivity of the electrodeposited MoS2 film. ACS Appl. Mater. Interfaces 10 (16), 13509–13518. https://doi.org/10.1021/acsami.8b01104.

An, L., Feng, J., Zhang, Y., Wang, R., Liu, H., Wang, G.-C., Cheng, F., Xi, P., 2019. Epitaxial heterogeneous interfaces on N-NiMoO4/NiS2 nanowires/nanosheets to boost hydrogen and oxygen production for overall water splitting. Adv. Funct. Mater. 29 (1), 1805298 https://doi.org/10.1002/adfm.201805298.

Anjum, M.A.R., Jeong, H.Y., Lee, M.H., Shin, H.S., Lee, J.S., 2018. Efficient hydrogen evolution reaction catalysis in alkaline media by all-in-one MoS2 with multifunctional active sites. Adv. Mater. 30 (20), 1707105 https://doi.org/10.1002/adma.201707105.

Beall, C.E., Fabbri, E., Schmidt, T.J., 2021. Perovskite oxide based electrodes for the oxygen reduction and evolution reactions: the underlying mechanism. ACS Catal. 11 (5), 3094–3114. https://doi.org/10.1021/acscatal.0c04473.

Burke, M.S., Enman, L.J., Batchellor, A.S., Zou, S., Boettcher, S.W., 2015. Oxygen evolution reaction electrocatalysis on transition metal oxides and (Oxy)hydroxides: activity trends and design principles. Chem. Mater. 27 (22), 7549–7558. https://doi.org/10.1021/acs.chemmater.5b03148.

Charles, H., Pawar, R.C., Khan, H., Chengula, P.J., Lee, C.S., 2023. Double-sided growth of MoSe2 nanosheets onto hollow zinc stannate (ZnO, ZnSnO3, and SnO2) nanofibers (h-ZTO) for efficient CO2 photoreduction. J. Environ. Chem. Eng. 11 (3), 109917 https://doi.org/10.1016/j.jece.2023.109917.

Chu, W., Shi, Z., Hou, Y., Ma, D., Bai, X., Gao, Y., Yang, N., 2020. Trifunctional of phosphorus-doped NiCo2O4 nanowire materials for asymmetric supercapacitor, oxygen evolution reaction, and hydrogen evolution reaction. ACS Appl. Mater. Interfaces 12 (2), 2763–2772. https://doi.org/10.1021/acsami.9b13182.

Claros, M., Setka, M., Jimenez, Y.P., Vallejos, S., 2020. AACVD synthesis and characterization of iron and copper oxides modified ZnO structured films. Nanomaterials.

Cui, M., Yang, C., Li, B., Dong, Q., Wu, M., Hwang, S., Xie, H., Wang, X., Wang, G., Hu, L., 2021. High-entropy metal sulfide nanoparticles promise high-performance oxygen evolution reaction. Adv. Energy Mater. 11 (3), 2002887 https://doi.org/10.1002/aenm.202002887.

Danyang, L., Liping, S., Qiang, L., Tian, X., Lihua, H., Hui, Z., 2022. High-entropy oxide (Fe0.2Zn0.2Co0.2Ni0.2Cu0.2)Fe2O4: an efficient and stable spinel-type electrocatalyst for H2O2 production in alkaline media. J. Alloys Compd. 913, 165148 https://doi.org/10.1016/j.jallcom.2022.165148.

Ding, S., Sun, Y., Lou, F., Yu, L., Xia, B., Duan, J., Zhang, Y., Chen, S., 2022. Plasma-regulated two-dimensional high entropy oxide arrays for synergistic hydrogen evolution: from theoretical prediction to electrocatalytic applications. J. Power Sources 520, 230873. https://doi.org/10.1016/j.jpowsour.2021.230873.

El-Refaei, S.M., Russo, P.A., Pinna, N., 2021. Recent advances in multimetal and doped transition-metal phosphides for the hydrogen evolution reaction at different pH values. ACS Appl. Mater. Interfaces 13 (19), 22077–22097. https://doi.org/10.1021/acsami.1c02129.

Fan, M.-Y., Wang, J.-J., Zhao, J., Zhang, H., Ma, T.-Y., Han, X.-P., Hu, W.-B., 2024. High-entropy oxide-supported platinum nanoparticles for efficient hydrogen evolution reaction. Rare Metals. https://doi.org/10.1007/s12598-023-02553-0.

Han, L., Dong, S., Wang, E., 2016. Transition-metal (Co, Ni, and Fe)-based electrocatalysts for the water oxidation reaction. Adv. Mater. 28 (42), 9266–9291. https://doi.org/10.1002/adma.201602270.

He, H., Kou, P., Zhang, Z., Wang, D., Zheng, R., Sun, H., Liu, Y., Wang, Z., 2024. Coupling high entropy oxide with hollow carbon spheres by rapid microwave solvothermal strategy for boosting oxygen evolution reaction. J. Colloid Interface Sci. 653, 179–188. https://doi.org/10.1016/j.jcis.2023.09.063.

He, L., Kang, H., Hou, G., Qiao, X., Jia, X., Qin, W., Wu, X., 2023. Low-temperature synthesis of nano-porous high entropy spinel oxides with high grain boundary density for oxygen evolution reaction. Chem. Eng. J. 460, 141675 https://doi.org/10.1016/j.cej.2023.141675.

Jin, S., 2017. Are metal chalcogenides, nitrides, and phosphides oxygen evolution catalysts or bifunctional catalysts? ACS Energy Lett. 2 (8), 1937–1938. https://doi.org/10.1021/acsenergylett.7b00679.

Kante, M.V., Weber, M.L., Ni, S., van den Bosch, I.C.G., van der Minne, E., Heymann, L., Falling, L.J., Gauquelin, N., Tsvetanova, M., Cunha, D.M., Koster, G., Gunkel, F., Nemšák, S., Hahn, H., Velasco Estrada, L., Baeumer, C., 2023. A high-entropy oxide as high-activity electrocatalyst for water oxidation. ACS Nano 17 (6), 5329–5339. https://doi.org/10.1021/acsnano.2c08096.

Li, B., Jiang, L., Li, X., Ran, P., Zuo, P., Wang, A., Qu, L., Zhao, Y., Cheng, Z., Lu, Y., 2017. Preparation of monolayer MoS2 quantum dots using temporally shaped femtosecond laser ablation of bulk MoS2 targets in water. Sci. Rep. 7 (1), 11182. https://doi.org/10.1038/s41598-017-10632-3.

Li, H., Lai, J., Li, Z., Wang, L., 2021. Multi-sites electrocatalysis in high-entropy alloys. Adv. Funct. Mater. 31 (47), 2106715 https://doi.org/10.1002/adfm.202106715.

Liang, H., Gandi, A.N., Anjum, D.H., Wang, X., Schwingenschlögl, U., Alshareef, H.N., 2016. Plasma-assisted synthesis of NiCoP for efficient overall water splitting. Nano Lett. 16 (12), 7718–7725. https://doi.org/10.1021/acs.nanolett.6b03803.

Lori, O., Zion, N., Honig, H.C., Elbaz, L., 2021. 3D metal carbide aerogel network as a stable catalyst for the hydrogen evolution reaction. ACS Catal. 11 (21), 13707–13713. https://doi.org/10.1021/acscatal.1c03332.

Lu, X.F., Yu, L., Zhang, J., Lou, X.W., 2019. Ultrafine dual-phased carbide nanocrystals confined in porous nitrogen-doped carbon dodecahedrons for efficient hydrogen evolution reaction. Adv. Mater. 31 (30), 1900699 https://doi.org/10.1002/adma.201900699.

Ma, N., Li, N., Wang, T., Ma, X., Fan, J., 2022. Strain engineering in the oxygen reduction reaction and oxygen evolution reaction catalyzed by Pt-doped Ti2CF2. J. Mater. Chem. A 10 (3), 1390–1401. https://doi.org/10.1039/D1TA07349D.

Ma, W., Ma, R., Wang, C., Liang, J., Liu, X., Zhou, K., Sasaki, T., 2015. A superlattice of alternately stacked Ni–Fe hydroxide nanosheets and graphene for efficient splitting of water. ACS Nano 9 (2), 1977–1984. https://doi.org/10.1021/nn5069836.

Mayhall, N.J., Becher, I.I.I.E.L., Chowdhury, A., Raghavachari, K., 2011. Molybdenum oxides versus molybdenum sulfides: geometric and electronic structures of Mo3Xy− (X = O, S and y = 6, 9) clusters. J. Phys. Chem. A 115 (11), 2291–2296. https://doi.org/10.1021/jp108344k.

Nagarajan, T., Khalid, M., Sridewi, N., Jagadish, P., Shahabuddin, S., Muthoosamy, K., Walvekar, R., 2022. Tribological, oxidation and thermal conductivity studies of microwave synthesized molybdenum disulfide (MoS2) nanoparticles as nano-additives in diesel based engine oil. Sci. Rep. 12 (1), 14108. https://doi.org/10.1038/s41598-022-16026-4.

Nguyen, T.X., Liao, Y.-C., Lin, C.-C., Su, Y.-H., Ting, J.-M., 2021. Advanced high entropy perovskite oxide electrocatalyst for oxygen evolution reaction. Adv. Funct. Mater. 31 (27), 2101632 https://doi.org/10.1002/adfm.202101632.

Noor, T., Yaqoob, L., Iqbal, N., 2021. Recent advances in electrocatalysis of oxygen evolution reaction using noble-metal, transition-metal, and carbon-based materials. ChemElectroChem. 8 (3), 447–483. https://doi.org/10.1002/celc.202001441.

Pan, Y., Xu, X., Zhong, Y., Ge, L., Chen, Y., Veder, J.-P.M., Guan, D., O'Hayre, R., Li, M., Wang, G., Wang, H., Zhou, W., Shao, Z., 2020. Direct evidence of boosted oxygen evolution over perovskite by enhanced lattice oxygen participation. Nat. Commun. 11 (1) https://doi.org/10.1038/s41467-020-15873-x, 2002.

Pawar, R.C., Chengula, P.J., Khan, H., Charles, H., Lee, C.S., 2023. Boosting photocatalytic CO2 conversion using strongly bonded Cu/reduced Nb2O5 nanosheets. Dalton Trans. 52 (36), 12832–12844. https://doi.org/10.1039/D3DT02082G.

Pawar, R.C., Kang, S., Khan, H., Han, H., Lee, C.S., 2021. Study of multi-faceted CoS2 introduced graphene aerogel hybrids via chemical approach for an effective electrocatalytic water splitting. Curr. Appl. Phys. 32, 78–85. https://doi.org/10.1016/j.cap.2021.10.002.

Pol, A., Sapakal, S., Khan, A., Kadam, A.V., 2023. Synthesis of NiO thin film on 304-grade stainless steel substrate for oxygen evolution reaction. Surf. Interfaces 37, 102706. https://doi.org/10.1016/j.surfin.2023.102706.

Rost, C.M., Sachet, E., Borman, T., Moballegh, A., Dickey, E.C., Hou, D., Jones, J.L., Curtarolo, S., Maria, J.-P., 2015. Entropy-stabilized oxides. Nat. Commun. 6 (1), 8485. https://doi.org/10.1038/ncomms9485.

Sha, S., Ge, R., Li, Y., Cairney, J.M., Zheng, R., Li, S., Liu, B., Zhang, J., Li, W., 2023. High-entropy catalysts for electrochemical water-electrolysis of hydrogen evolution and oxygen evolution reactions. Front. Energy. https://doi.org/10.1007/s11708-023-0892-6.

Shaikh, J.S., Rittiruam, M., Saelee, T., Márquez, V., Shaikh, N.S., Khajondetchairit, P., Pathan, S.C., Jiraborvornpongsa, N., Praserthdam, S., Praserthdam, P., 2023a. High entropy materials frontier and theoretical insights for logistics CO2 reduction and hydrogenation: electrocatalysis, photocatalysis and thermo-catalysis. J. Alloys Compd. 969, 172232 https://doi.org/10.1016/j.jallcom.2023.172232.

Shaikh, J.S., Rittiruam, M., Saelee, T., Márquez, V., Shaikh, N.S., Santos, J.S., Kanjanaboos, P., Nazeeruddin, M.K., Praserthdam, S., Praserthdam, P., 2022. Ru tailored hydrous cobalt phosphate as a rational approach for high-performance alkaline oxygen evolution reaction. Mater. Today Chem. 26, 101267 https://doi.org/10.1016/j.mtchem.2022.101267.

Shaikh, N.S., Shaikh, J.S., Márquez, V., Pathan, S.C., Mali, S.S., Patil, J.V., Hong, C.K., Kanjanaboos, P., Fontaine, O., Tiwari, A., Praserthdam, S., Praserthdam, P., 2023b. New perspectives, rational designs, and engineering of Tin (Sn)-based materials for electrochemical CO2 reduction. Mater. Today Sustain. 22, 100384 https://doi.org/10.1016/j.mtsust.2023.100384.

Shi, Y., Zhang, B., 2016. Recent advances in transition metal phosphide nanomaterials: synthesis and applications in hydrogen evolution reaction. Chem. Soc. Rev. 45 (6), 1529–1541. https://doi.org/10.1039/C5CS00434A.

Sun, L., Luo, Q., Dai, Z., Ma, F., 2021. Material libraries for electrocatalytic overall water splitting. Coord. Chem. Rev. 444, 214049 https://doi.org/10.1016/j.ccr.2021.214049.

Suryanto, B.H.R., Wang, Y., Hocking, R.K., Adamson, W., Zhao, C., 2019. Overall electrochemical splitting of water at the heterogeneous interface of nickel and iron oxide. Nat. Commun. 10 (1), 5599. https://doi.org/10.1038/s41467-019-13415-8.

Suturin, S.M., Korovin, A.M., Bursian, V.E., Lutsev, L.V., Bourobina, V., Yakovlev, N.L., Montecchi, M., Pasquali, L., Ukleev, V., Vorobiev, A., Devishvili, A., Sokolov, N.S., 2018. Role of gallium diffusion in the formation of a magnetically dead layer at the ${\mathrm{Y}}_{3}{\mathrm{Fe}}_{5}{\mathrm{O}}_{12}/{\mathrm{Gd}}_{3}{\mathrm{Ga}}_{5}{\mathrm{O}}_{12}$ epitaxial interface. Phys. Rev. Mater. 2 (10), 104404 https://doi.org/10.1103/PhysRevMaterials.2.104404.

Svane, K.L., Rossmeisl, J., 2022. Theoretical optimization of compositions of high-entropy oxides for the oxygen evolution reaction**. Angew. Chem. Int. Ed. 61 (19), e202201146 https://doi.org/10.1002/anie.202201146.

Talluri, B., Yoo, K., Kim, J., 2022. High entropy spinel metal oxide (CoCrFeMnNi)3O4 nanoparticles as novel efficient electrocatalyst for methanol oxidation and oxygen evolution reactions. J. Environ. Chem. Eng. 10 (1), 106932 https://doi.org/10.1016/j.jece.2021.106932.

Wang, C., Li, C., Liu, J., Guo, C., 2021b. Engineering transition metal-based nanomaterials for high-performance electrocatalysis. Mater. Rep.: Energy 1 (1), 100006. https://doi.org/10.1016/j.matre.2021.01.001.

Wang, D., Jiang, S., Duan, C., Mao, J., Dong, Y., Dong, K., Wang, Z., Luo, S., Liu, Y., Qi, X., 2020. Spinel-structured high entropy oxide (FeCoNiCrMn)3O4 as anode towards superior lithium storage performance. J. Alloys Compd. 844, 156158 https://doi.org/10.1016/j.jallcom.2020.156158.

Wang, D., Liu, Z., Du, S., Zhang, Y., Li, H., Xiao, Z., Chen, W., Chen, R., Wang, Y., Zou, Y., Wang, S., 2019. Low-temperature synthesis of small-sized high-entropy oxides for water oxidation. J. Mater. Chem. A 7 (42), 24211–24216. https://doi.org/10.1039/C9TA08740K.

Wang, J., Zhang, M., Yang, G., Song, W., Zhong, W., Wang, X., Wang, M., Sun, T., Tang, Y., 2021a. Heterogeneous bimetallic Mo-NiPx/NiSy as a highly efficient electrocatalyst for robust overall water splitting. Adv. Funct. Mater. 31 (33), 2101532 https://doi.org/10.1002/adfm.202101532.

Wu, G., Santandreu, A., Kellogg, W., Gupta, S., Ogoke, O., Zhang, H., Wang, H.-L., Dai, L., 2016. Carbon nanocomposite catalysts for oxygen reduction and evolution reactions: from nitrogen doping to transition-metal addition. Nano Energy 29, 83–110. https://doi.org/10.1016/j.nanoen.2015.12.032.

Wu, L., Shen, X., Ji, Z., Yuan, J., Yang, S., Zhu, G., Chen, L., Kong, L., Zhou, H., 2023. Facile synthesis of medium-entropy metal sulfides as high-efficiency electrocatalysts toward oxygen evolution reaction. Adv. Funct. Mater. 33 (3), 2208170 https://doi.org/10.1002/adfm.202208170.

Wu, Z., Zhao, Y., Jin, W., Jia, B., Wang, J., Ma, T., 2021. Recent progress of vacancy engineering for electrochemical energy conversion related applications. Adv. Funct. Mater. 31 (9), 2009070 https://doi.org/10.1002/adfm.202009070.

Xiong, Y., Xu, L., Jin, C., Sun, Q., 2019. Interface-engineered atomically thin Ni3S2/MnO2 heterogeneous nanoarrays for efficient overall water splitting in alkaline media. Appl. Catal. B: Environ. 254, 329–338. https://doi.org/10.1016/j.apcatb.2019.05.017.

Yan, D., Xia, C., Zhang, W., Hu, Q., He, C., Xia, B.Y., Wang, S., 2022. Cation defect engineering of transition metal electrocatalysts for oxygen evolution reaction. Adv. Energy Mater. 12 (45), 2202317 https://doi.org/10.1002/aenm.202202317.

Yang, Y., Zhang, K., Lin, H., Li, X., Chan, H.C., Yang, L., Gao, Q., 2017. MoS2–Ni3S2 heteronanorods as efficient and stable bifunctional electrocatalysts for overall water splitting. ACS Catal. 7 (4), 2357–2366. https://doi.org/10.1021/acscatal.6b03192.

Yin, J., Jin, J., Lin, H., Yin, Z., Li, J., Lu, M., Guo, L., Xi, P., Tang, Y., Yan, C.-H., 2020. Optimized metal chalcogenides for boosting water splitting. Adv. Sci. 7 (10), 1903070 https://doi.org/10.1002/advs.201903070.

You, J., Yao, R., Ji, W., Zhao, Y., Wang, Z., 2022. Research of high entropy alloys as electrocatalyst for oxygen evolution reaction. J. Alloys Compd. 908, 164669 https://doi.org/10.1016/j.jallcom.2022.164669.

Yu, N., Zhang, Z.-J., Chai, Y.-M., Dong, B., 2023. Regulation engineering of the surface and structure of perovskite-based electrocatalysts for the oxygen evolution reaction. Mater. Chem. Front. https://doi.org/10.1039/D3QM00438D.

Zhang, J., Wang, T., Pohl, D., Rellinghaus, B., Dong, R., Liu, S., Zhuang, X., Feng, X., 2016. Interface engineering of MoS2/Ni3S2 heterostructures for highly enhanced electrochemical overall-water-splitting activity. Angew. Chem. Int. Ed. 55 (23), 6702–6707. https://doi.org/10.1002/anie.201602237.

Zhang, Q., Hu, Y., Wu, H., Zhao, X., Wang, M., Wang, S., Feng, R., Chen, Q., Song, F., Chen, M., Liu, P., 2023. Entropy-stabilized multicomponent porous spinel nanowires of NiFeXO4 (X = Fe, Ni, Al, Mo, Co, Cr) for efficient and durable electrocatalytic oxygen evolution reaction in alkaline medium. In: ACS Nano, 17, pp. 1485–1494. https://doi.org/10.1021/acsnano.2c10247.

Zhu, J., Wang, Z.-C., Dai, H., Wang, Q., Yang, R., Yu, H., Liao, M., Zhang, J., Chen, W., Wei, Z., Li, N., Du, L., Shi, D., Wang, W., Zhang, L., Jiang, Y., Zhang, G., 2019. Boundary activated hydrogen evolution reaction on monolayer MoS2. Nat. Commun. 10 (1), 1348. https://doi.org/10.1038/s41467-019-09269-9.